Towards Direct Reconstruction from a Gamma Camera Based on Compton Scattering

Michael J. Cree and Philip J. Bones

Abstract—The Compton scattering camera (sometimes called the electronically collimated camera) has been shown by others to have the potential to better the photon counting statistics and the energy resolution of the Anger camera for imaging in SPECT. By using coincident detection of Compton scattering events on two detecting planes, a photon can be localized to having been sourced on the surface of a cone. New algorithms are needed to achieve fully three-dimensional reconstruction of the source distribution from such a camera. If a complete set of cone-surface projections are collected over an infinitely extending plane, it is shown that the reconstruction problem is not only analytically solvable, but also overspecified in the absence of measurement uncertainties. Two approaches to direct reconstruction are proposed, both based on the photons which travel perpendicularly between the detector planes. Results of computer simulations are presented which demonstrate the ability of the algorithms to achieve useful reconstructions in the absence of measurement uncertainties (other than those caused by quantization). The modifications likely to be required in the presence of realistic measurement uncertainties are discussed.

I. INTRODUCTION

NUCLEAR MEDICAL IMAGING is an important tool for diagnostic purposes, particularly since information gained contains a physiological component which is not obtainable with most other imaging modalities. However, the dangers to the patient of administered radiopharmaceuticals coupled with the difficulty of imaging gamma-photons have limited the development of detection systems. Since its development over 30 years ago, the Anger camera [1] has remained the major image formation device in nuclear medicine. While some improvements in spatial and energy resolution have been achieved over this period, the need for a physical (lead) collimator places a severe limit on performance [2, 3]. The presence of the collimator also necessitates the rotation of the Anger camera for performing single photon emission computed tomography (SPECT). It is for these reasons we consider the proposal by Singh [4] of utilizing Compton scattering in the detection process to achieve photon directional localization significant. Singh [4] refers to such a detector as an electronically collimated camera, however we prefer the term 'Compton scattering camera'. This is in line with astronomical terminology, where a similar device called the

Compton scattering telescope (or Compton telescope) is used for high energy X-ray imaging of the sky [5].

The nature of directional localization in the Compton scattering camera (described in detail below) necessitates the development of new reconstruction algorithms. The algorithms already developed for astronomical imaging will not suffice since they are based on an assumed two-dimensional source distribution, the 'sky'. Required instead are algorithms to achieve fully three-dimensional reconstruction of the gamma-ray source distribution, in principle without movement of the detector system. Singh, et. al. [6, 7] have chosen to develop iterative algorithms with which they have had some success [8]. Their reasons for choosing iterative algorithms are that direct reconstruction is more difficult in this case than for conventional computed tomography (CT) and that the measurements are photon-limited. However, it is often difficult to know with iterative techniques at which point convergence has been achieved (or indeed if it has been achieved) and results are often only achieved at considerable computational expense. In conventional CT systems, direct reconstruction methods have found great success and are often the preferred choice of algorithm. For these reasons we have chosen to examine the possibility of using direct three-dimensional reconstruction in application to the Compton scattering camera. This examination forms the main bulk of this paper.

A brief review of the principle of operation of the Compton scattering camera is given in the next section. Then in Section III the formation of 'cone-surface projections' is formulated. In Section IV it is shown that the equations for a certain selection of cone-surface projections can be inverted analytically to give the three-dimensional source distribution. Furthermore, an equation linking the same selection of cone-surface projections to parallel-ray projections is derived. Two possible reconstruction paths—one directly reconstructing the source and the other a two-stage reconstruction using already established cone-beam reconstruction algorithms—are thus suggested. In Section V we report the results of our discretized implementation of the two algorithms for almost perfect (thus unrealistic) data. The data collected by any practical Compton scattering camera will be photon-limited as well as having limited energy and angular resolution; the algorithms described will undoubtedly need modifications therefore for use with a practical camera. Possible modifications are discussed in Section VI.

II. THE COMPTON SCATTERING CAMERA

The Compton scattering camera consists of two detecting planes (see Fig. 1(a)). The first detector, closest to the source
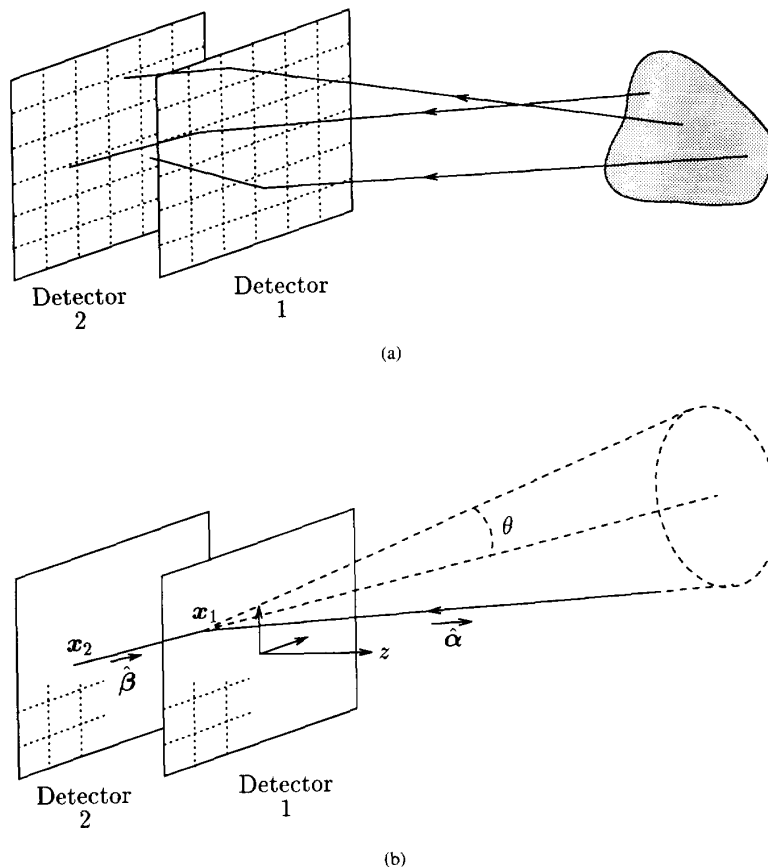
(a)

(b)

Fig. 1. Geometry of the Compton scattering camera: (a) Photons emitted from a gamma source are scattered in detector 1 and absorbed in detector 2. (b) The backprojection for a particular trajectory through x_1 and x_2 with scattering angle θ localizes the photon as having been sourced somewhere on the surface of a cone (dotted line).

distribution, is designed so that Compton scattering is the dominant interaction process while the second detector is designed so that complete absorption of photons takes place [4]. The idea is that a photon incident on the camera is reasonably likely to undergo Compton scattering in the first detector, wherein the position and energy of the interaction are measured, then be absorbed in the second detector, wherein the position and energy of absorption are measured. In practice detector 1 is most likely to be a semiconductor array [4], [9], [10], while detector 2 could be either another semiconductor array or an Anger camera without a collimator. For simplicity the detector planes are depicted as planar arrays in Fig. 1. The angle of Compton scatter in the first detector can be calculated from the deposit of energy ΔE by

$$\cos\theta = 1 - \frac{mc^2\Delta E}{(E - \Delta E)E} \qquad (1)$$

where E is the initial photon energy, m is the electronic mass, and c is the velocity of light [11]. Since the initial photon energy E is fixed by the choice of radiopharmaceutical, it is possible to use the measured photon energy, $E_m = \Delta E + E_2$, where E_2 is the energy deposited in detector 2, to discriminate against photons from other sources (background radiation) and

those photons from the source of interest which may have experienced scatter before reaching the camera. Other SPECT techniques also have to make this discrimination.

From the two position measurements and angle of scatter, one can back-project to localize the photon as having been sourced on the surface of a cone whose apex lies at the point of Compton scatter, x_1, has semiangle θ and axis of symmetry passing through the two detection points, x_1 and x_2 (see Fig. 1(b)). Since this process of photon directional localization does not limit photons to fixed parallel paths, we think it inappropriate to describe it as 'electronic collimation'; we prefer the description 'Compton scattering camera'.

Some variants of the arrangement described above have been reported. For example, Everett et. al. [12] and Kamae et. al. [13] both describe a device for tracking the photon through multiple Compton interactions, but use only the first two interactions in the same manner as described above. Dogan et. al. [14] show that by considering polarization of photons during multiple Compton scattering, directional localization can be refined to be better than the surface of a cone. Their results were developed for a localized source and need to be generalized before being applicable to a three-dimensional source distribution.

While the Compton scattering camera obviates the need for the highly inefficient collimator of the Anger camera, it does have severe limitations of its own. The energy discrimination in the first detector limits the resolution in scattering angle and this resolution is itself dependent on the angle [9]. The detector elements in both arrays must necessarily be of finite sectional area and thickness and finite in number. They also cannot abut one another perfectly (i.e. there must be some fraction of the detector volume in which no detection occurs). Thus neither x_1 nor x_2 can be determined with great precision so that the axis of the cone on which a given photon is sourced is only imprecisely determined. Finally, only those photons for which unambiguous coincidence in the two detectors occurs can be used in forming images. Solomon and Ott [9] have studied these factors and conclude that despite the limitations, a practical Compton scattering camera can be expected to offer an intrinsic efficiency of approximately 2% and a FWHM of about 3 mm over an energy range of 100 KeV to 1 MeV. These characteristics seem very competitive with current Anger camera technology.

III. CONE-SURFACE PROJECTIONS

In the previous section it is shown that the back-projection of a photon detection event leads to the localization of the photon's source as being on the surface of a cone. If many photon events are measured, the number of photon counts characterized by a certain x_1, x_2 and θ will be approximately proportional to the integration of the photon source distribution over the surface of the cone defined by x_1, x_2 and θ. This measurement, labelled $\lambda(x_1, \hat{\beta}, \theta)$, is called herein the cone-surface projection. The unit vector $\hat{\beta}$ is directed from x_2 to x_1, where x_1 is taken to span the space which the detector covers (see Fig. 1(b)). Normally this would be a plane as shown, however a geometry such as a spherical surface is not inconceivable. We develop results for x_1 spanning an infinite plane only.

To develop an integral formulation of λ for the cone-surface projection, the disembodied X-ray source distribution, μ, is required to be a continuous, differentiable, positive real function of space with compact support. The first detector surface is taken to extend over the xy-plane of the coordinate system with the source function nonzero for positive z values only. The unit vector $\hat{\alpha}$ is defined by $\hat{\alpha} \cdot \hat{\beta} = \cos\theta$, thus is a function of $\hat{\beta}$, θ and one other parameter, say ϕ. From its definition, $\hat{\alpha}$ can be seen to be always directed from the apex of the cone along the surface of the cone (see Fig. 1(b)). With respect to the cone's axis, θ and ϕ are the polar and azimuthal angles respectively describing $\hat{\alpha}$, thus $\hat{\alpha} = \hat{\alpha}(\hat{\beta}, \theta, \phi)$. The distance from the apex to any point on the cone with nonnegative z coordinate is r. The cone-surface projection is then

$$\lambda(x_1, \hat{\beta}, \theta) = K(\theta) \int_0^{2\pi} \int_0^{\infty} \mu(x_1 + \hat{\alpha}r) r \sin\theta \, dr \, d\phi \quad (2)$$

where the Klein-Nishina distribution for Compton scattering [11] and any constants such as detector efficiency have been incorporated into the $K(\theta)$ factor. The complicated depen-

dence of $\hat{\alpha}$ on $\hat{\beta}$ suggests that (2) is not invertible by linear analytic methods. Thus we consider below a subset of all the cone-surface projections—those that satisfy $\hat{\beta} = \hat{z}$. This is equivalent to inserting a parallel hole collimator between the two detectors of the Compton scattering camera. While limiting the sensitivity of the camera this enables the inversion of (2) (with $\hat{\beta} = \hat{z}$). Possible means of generalization to all projections are discussed in Section VI.

We re-express the cone-surface projection as $\lambda(x, y, \theta)$ where $x_1 = (x, y, 0)$ and $\hat{\beta}$ is now assumed to be identical to $\hat{z}$, thus

$$\lambda(x, y, \theta) = K(\theta)$$
$$\times \int_0^{2\pi} \int_0^{\infty} \mu(x + r\alpha_x, y + r\alpha_y, r\alpha_z) r \sin\theta \, dr \, d\phi. \quad (3)$$

Now $\hat{\alpha} = (\alpha_x, \alpha_y, \alpha_z) = (\sin\theta\cos\phi, \sin\theta\sin\phi, \cos\theta)$ and $z = r\cos\theta$, thus

$$\lambda(x, y, \theta) = K(\theta) \frac{\sin\theta}{\cos^2\theta}$$
$$\times \int_0^{2\pi} \int_0^{\infty} \mu(x + z\tan\theta\cos\phi, y + z\tan\theta\sin\phi, z) z \, dz \, d\phi. \quad (4)$$

In the inversion process the quantity $\tan\theta$ is involved in an integral transform so it is convenient to take $t = \tan\theta$ and re-express all functions of θ in terms of t to give the final form of the cone-surface projection as

$$\lambda(x, y, t) = K(t) t \sqrt{1 + t^2}$$
$$\times \int_0^{2\pi} \int_0^{\infty} \mu(x + zt\cos\phi, y + zt\sin\phi, z) z \, dz \, d\phi \quad (5)$$

which is subsequently referred to as the restricted cone-surface projection, i.e., the cone-surface projection for which $\hat{\beta} = \hat{z}$.

IV. INVERSION OF RESTRICTED CONE-SURFACE PROJECTIONS

The inversion is performed in Fourier space and to this end $\mathcal{F}_2$ is defined to be the two-dimensional Fourier transform operator, thus

$$\Lambda_2(u, v, t) = \mathcal{F}_2[\lambda(x, y, t)]$$
$$= \int_{-\infty}^{\infty} \int_{-\infty}^{\infty} \lambda(x, y, t) \exp(-i2\pi(ux + vy)) dx \, dy \quad (6)$$

$$M_2(u, v, z) = \mathcal{F}_2[\mu(x, y, z)]$$
$$= \int_{-\infty}^{\infty} \int_{-\infty}^{\infty} \mu(x, y, z) \exp(-i2\pi(ux + vy)) dx \, dy. \quad (7)$$

Letting $\mathcal{F}$ act on both sides of (5) with invocation of the Fourier shift theorem gives

$$\Lambda_2(u, v, t) = K(t) t \sqrt{1 + t^2}$$
$$\times \int_0^{2\pi} \int_0^{\infty} M_2(u, v, z) \exp\{i2\pi zt(u\cos\phi + v\sin\phi)\} z \, dz \, d\phi. \quad (8)$$

If we had not chosen $\hat{\beta} = \hat{z}$ then M_2 would still have some ϕ dependence which would make the next step impossible, which is to evaluate the ϕ-integral. By expressing the rectangular coordinate pair (u, v) in terms of the polar coordinate pair (ρ, ψ) in (8), the ϕ-integral is recognizable as the standard integral definition of the zero-order Bessel function of the first kind, namely

$$J_0(\gamma) = \frac{1}{2\pi} \int_0^{2\pi} e^{i\gamma \cos \phi} d\phi \qquad (9)$$

where $\gamma = 2\pi z t\rho$, and thus

$$\Lambda_2(u, v, t) = K(t)t\sqrt{1 + t^2}\, 2\pi$$
$$\times \int_0^\infty M_2(u, v, z) J_0(2\pi z t \sqrt{u^2 + v^2}) z\, dz. \qquad (10)$$

The z-integral is a zero-order Hankel transform acting on M_2. Defining

$$\mathcal{H}_0[\ ](r \to \rho) = 2\pi \int_0^\infty [\ ] r J_0(2\pi r\rho) dr \qquad (11)$$

to be the zero-order Hankel transform and letting $\xi = z\sqrt{u^2 + v^2}$ allows (10) to be rewritten as

$$\Lambda_2(u, v, t) = \frac{K(t)t\sqrt{1 + t^2}}{u^2 + v^2}$$
$$\times \mathcal{H}_0\left[M_2\left(u, v, \frac{\xi}{\sqrt{u^2 + v^2}}\right)\right](\xi \to t). \quad (12)$$

The Hankel transform is self reciprocal so

$$M_2\left(u, v, \frac{\xi}{\sqrt{u^2 + v^2}}\right) = \mathcal{H}_0\left[\frac{u^2 + v^2}{K(t)t\sqrt{1 + t^2}} \Lambda_2(u, v, t)\right](t \to \xi) \qquad (13)$$

where care must be taken to exclude $t = 0$.

An inverse Fourier transform will give μ, however the transform must be performed on the surface defined by $z = \frac{\xi}{\sqrt{u^2 + v^2}}$ in (u, v, z) space. We arrive at:

Theorem 1: From a complete set of restricted cone-surface projections, that is, $\lambda(x, y, t)$ for $(x, y) \in R^2$ and $t \in [0, \infty)$, the X-ray source distribution $\mu(x, y, z)$ can be reconstructed.

The reconstruction may be performed by invoking (6), then (13) and then the inverse Fourier transform with the special provisions mentioned above.

The possibility of relating cone-surface projections to the more conventional cone-beam projections is appealing. That this possibility exists is indicated by Singh and Doria's two stage iterative algorithm [6] where the (x, y)-detector space is pixellated and cone-beam projections are formed for each pixel. Let us then consider the definition of the cone-beam projection, which is [15]

$$g(x_1, \hat{\beta}) = \int \mu(x_1 + \hat{\beta} r) dr \qquad (14)$$

using the x_1, $\hat{\beta}$ notation as developed in section III. The same difficulty with allowing $\hat{\beta}$ to be arbitrary is anticipated, so the usual restriction $\hat{\beta} = \hat{z}$ is made to give the parallel-ray projection perpendicular to the camera aperture plane, which is

$$p_z(x, y) = g((x, y, 0), \hat{z}) \qquad (15)$$
$$= \int \mu(x, y, z) dz \qquad (16)$$

and x_1 again is taken to span the plane $(x, y, 0)$. We seek to find the $p_z(x, y)$ in terms of the $\lambda(x, y, t)$. The first step is to manipulate (5) and integrate with respect to t to give

$$\int_0^\infty \frac{\lambda(x, y, t)}{K(t)t\sqrt{1 + t^2}} dt = \int_0^\infty \int_0^{2\pi} \int_0^\infty \mu(x + tz \cos \phi, y + tz \sin \phi, z) z\, dz\, d\phi\, dt \qquad (17)$$

and transform to Fourier space,

$$\mathcal{F}_2\left[\int_0^\infty \frac{\lambda(x, y, t)}{K(t)t\sqrt{1 + t^2}} dt\right]$$
$$= \int_0^\infty \int_0^{2\pi} \int_0^\infty M_2(u, v, z) e^{i2\pi zt(u \cos \phi + v \sin \phi)} z\, dz\, d\phi\, dt$$
$$= 2\pi \int_0^\infty \int_0^\infty M_2(u, v, z) J_0(2\pi tz \sqrt{u^2 + v^2}) z\, dz\, dt$$
$$= \frac{1}{\sqrt{u^2 + v^2}} \int_0^\infty M_2(u, v, z) dz$$
$$= \frac{1}{\sqrt{u^2 + v^2}} \mathcal{F}_2[p_z]. \qquad (18)$$

Rearranging (taking care to exclude the point $u = v = 0$), returning to function space and invoking the convolution theorem gives

$$p_z(x, y) = \frac{-1}{(2\pi)^2 (x^2 + y^2)^{\frac{3}{2}}} \odot \int_0^\infty \frac{\lambda(x, y, t)}{K(t)t\sqrt{1 + t^2}} dt \quad (19)$$

where $\odot$ is the convolution operator and

$$\mathcal{F}_2^{-1}\left[\sqrt{u^2 + v^2}\right] = \frac{-1}{(2\pi)^2 (x^2 + y^2)^{\frac{3}{2}}}. \qquad (20)$$

A question remains as to whether the integral in (19) is well behaved. Consider the limit as $t \to 0$ of both sides of (5),

$$\lim_{t \to 0} \lambda(x, y, t) = \lim_{t \to 0}\left[K(t)t\sqrt{1 + t^2}\right.$$
$$\left. \cdot \int_0^\infty \int_0^{2\pi} \mu(x + tz \cos \phi, y + tz \sin \phi, z) z\, dz\, d\phi\right]$$
$$= 0 \cdot 2\pi \int_0^\infty \mu(x, y, z) z\, dz. \qquad (21)$$

We argue that the remaining integral on the right-hand side is finite for μ of finite support. Therefore $\lim_{t \to 0} \frac{\lambda(x, y, t)}{K(t)t\sqrt{1 + t^2}}$ is also finite and the integral in (19) exists.

Theorem 2: The parallel-ray projection perpendicular to the camera aperture plane, $p_z(x, y)$, can be calculated from knowledge of the complete set of restricted cone-surface projections.

Such a process is indicated by (19). To enable reconstruction of the entire three-dimensional source distribution, all cone-beam projections for general $\hat{\beta}$ are needed, therefore (19), in itself, is not enough to enable reconstruction to proceed. For cone-beam reconstruction to have a unique solution, it has been shown [15] that every plane which intersects the source distribution must intersect detector 1; an infinitely extending plane (as close as practicable to the source) does satisfy this condition, confirming that a direct three-dimensional reconstruction is feasible without having to rotate or translate the detector system. Discussion relating to possible means of generalizing (19) is left to Section VI. In the following section we present the results of testing our numerical implementations of (13) and (19).

V. RESULTS OF COMPUTER SIMULATION

We examine the discretization of (13) and (19) in turn and report the results of testing for some simple test functions. The suitability of the equations for machine computation is under consideration and to this end a good camera under ideal situations has been simulated. In particular, the cone-surface projection integral is assumed exact and the effects of low photon counts are ignored in the treatment. For the point source, discussed below, the effects of angular uncertainty due to the scattering detector finite energy resolution are included.

Three different sources are tested, namely a point source, a set of point sources and a uniform spherical distribution. For a point source located at (a, b, c), the restricted set of cone-surface projections is

$$\lambda(x, y, t) = \sqrt{1 + t^2}\delta\left(\sqrt{(x - a)^2 + (y - b)^2} - ct\right). \quad (22)$$

The advantage of the point source is that it can be carried through the complete reconstruction process analytically, enabling the machine computation to be checked thoroughly. Equation (22) is used to generate the single and multiple point source configurations. For a uniform spherical source of unit intensity, radius R and located at $(0, 0, a)$, the ϕ-integral of the cone-surface projection can be evaluated to give (23) (see equation at the bottom of the page) where $r = \sqrt{x^2 + y^2}$. The final integral does not lend itself to analytical evaluation so numerical integration has been used to calculate the projections.

Although the cone-surface projections, by theorem 1, should be calculated over all (x, y)-space and for all $t \in [0, \infty)$, this is impractical for machine computation. Instead, the face of detector 1 is made 10×10 units in size in the (x, y)-space (centered on the origin) and divided into $N \times N$ square pixels. The unit size is just a means of making quantitative comparisons of relative sizes without having to fix a specific
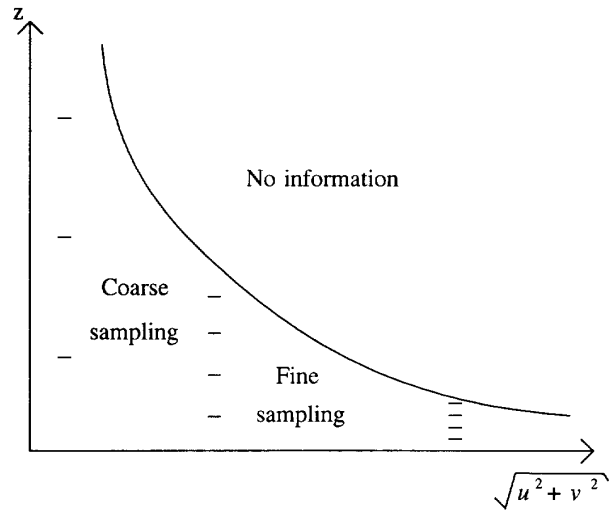

Fig. 2. Location of samples in (u, v, z)-space. After the Hankel transform has been performed samples are unevenly spaced in (u, v, z)-space and interpolation with respect to z is needed to give evenly spaced samples in a plane for constant z.

measurement system. Outside the area covered by the detectors the projections are assumed to be identically zero. The t-space is likewise divided into K evenly spaced samples ranging from $t_{\min} = 0$ to $t_{\max} = 3.2$. The value of $t_{\max}$ is significant in that it corresponds roughly to $70°$, a value which Singh et. al. [6] report as being about the maximum measurable angle for their prototype Compton scattering camera. The evenly spaced samples in t lead to unevenly spaced samples in the angular coordinate θ; this turns out to be beneficial (although not optimal) since the nature of Compton scattering gives better angular resolution for larger deflections of the photon. The Compton scattering camera is not physically capable of measuring the projection data for t near 0 (since no detection means no energy deposition and energy resolution is significantly restricted in any practical detector), hence the $t = 0$ projection has been assumed to be zero in the simulations.

Having estimated the cone-surface projections we proceed to examine the discretization of (13). The initial and final Fourier transforms can be easily evaluated with the fast Fourier transform (FFT). The scaling by $u^2 + v^2$ in the Fourier domain is modified at high frequencies (just as the conventional 'rho-filter' is in computed tomography, see for example [16]), which is particularly necessary for noisy data. A variety of algorithms exist for the computation of the Hankel transform [17], [18]. As speed is not an issue in the simulation, simple trapezoidal integration has been used since it was found to be most reliable for a broad range of input functions [18]. The algorithm in use gives K evenly spaced ξ samples ranging from $\xi_{\min} = 0$ to $\xi_{\max} = (K - 1)/2t_{\max}$ (refer to (13). The relationship $\xi = z\sqrt{u^2 + v^2}$ results in Fourier space sampling

$$\lambda(x, y, t) = 2t\sqrt{1 + t^2} \int_{a-R}^{a+R} \left[\pi - \cos^{-1}\left(\frac{R^2 - r^2 - a^2}{2zrt} + \frac{a}{2rt} - \frac{(1 + t^2)z}{2rt}\right)\right] z\,dz \quad (23)$$
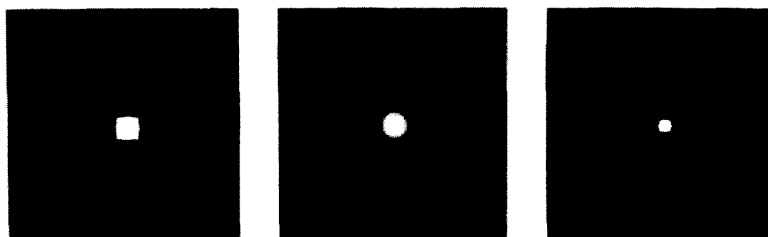
Fig. 3. Reconstruction of a point source showing xy-plane. The point source is located at $(0,0,5$ units) with the xy-plane located at $z = 5$ units shown. Left: $N = 32, K = 32$ (i.e. $N \times N$ spatial samples with K angular samples). Center: $N = 64, K = 32$. Right: $N = 64, K = 64$.
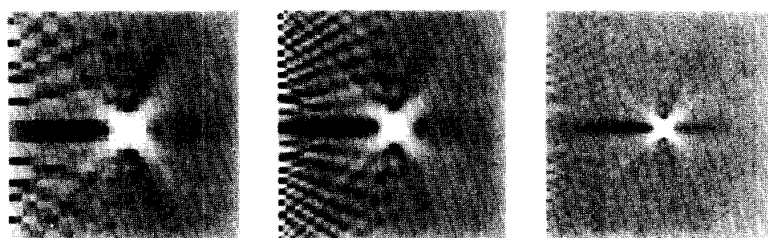

Fig. 4. Reconstruction of a point source showing zx-plane. The point source is located at $(0,0,5$ units) with the zx-plane located at $y = 0$ shown. Left: $N = 32, K = 32$. Center: $N = 64, K = 32$. Right: $N = 64, K = 64$.

as shown in Fig. 2. Notable is the coarse sampling at low frequencies and the finer sampling at high frequencies with a frequency cutoff along the curve $z = \frac{\xi_{max}}{\sqrt{u^2+v^2}}$. This means that for a planar reconstruction parallel to the detector face, $M_2(u,v,z)$ is limited to a decreasing range of u, v values as z is increased. Thus the spatial resolution of the camera decreases for increasing distance away from the front detector plane. The uneven sampling in (u,v,z)-space necessitates one-dimensional interpolation with respect to z to allow the FFT to be used to perform the final inverse Fourier transform. We use simple linear interpolation to obtain information at the necessary sampling points. Above the frequency cutoff, samples are assumed to be zero.

Reconstruction simulations were performed for the three source configurations on three different grid schemes: with $N = 32, K = 32$, with $N = 64, K = 32$ and with $N = 64, K = 64$. Figs. 3 and 4 show reconstructions of a point source located at $(0,0,5$ units) for the three grid schemes. Note that the source itself is better resolved as the sampling frequencies in space and angle are increased. It is noticeable in Fig. 4, however, that artifacts near the detector face are more pronounced for the $N = 64$, $K = 32$ grid configuration. We believe the causes of the artifacts to be the coarse (though realistic) quantization in angle and the simple interpolation scheme employed in Fourier space. The artifacts are located well away from the source. Blurring the projections to model the angular uncertainty of a real detector helps to reduce the artifacts. The images of Figs. 3 and 4 are calculated with an

TABLE I
RESOLUTION OBTAINABLE WITH ALGORITHM 1

Number of Samples	xy resolution		z resolution	
(N,K)	$z=3$	$z=6$	$z=3$	$z=6$
32, 32	1.0	1.3	0.5	1.8
64, 32	0.7	1.3	0.5	1.8
64, 64	0.5	0.7	0.3	1.0

angular uncertainty consistent with a detector energy resolution of 1keV (FWHM) and initial photon energy of 140 keV.

Fig. 5 shows reconstructions for multiple point sources lying in the zx-plane at different distances away from the camera. The effect of loss of position resolution for increasing z is clearly visible, as is the loss of intensity. Both effects are due to the loss of Fourier space sampling mentioned above. A series of tests with two point sources close together was performed to establish the spatial resolution possible. The spatial resolution is taken to be the distance apart two point sources must be placed so that the saddle point in the estimated image function is lower than 50% of the average of the peak amplitudes. Table I lists the resolution obtainable at distances of $z = 3$ and $z = 6$ from the camera for the different grid schemes.

Figs. 6 and 7 show the reconstruction of a uniform spherical source of radius $R = 1$ unit at the position $(0,0,5$ units). In the xy-planes (Fig. 6) the reconstruction is very good, despite the fact that the measurement for $t = 0$ is assumed to be zero. In the zx-planes (Fig. 7) some distortion is evident, primarily due to the truncation of projections by the finite size of the
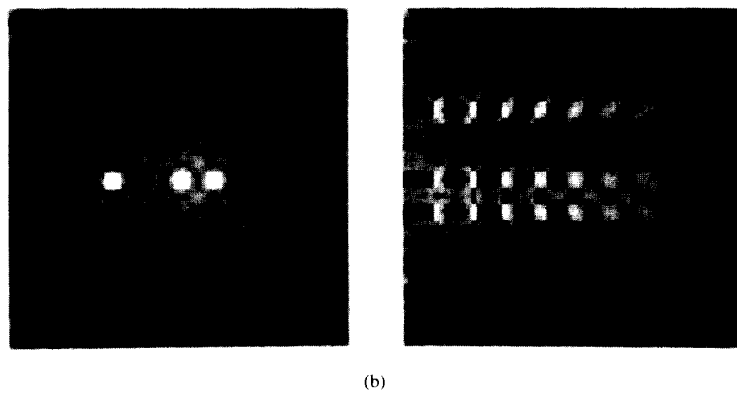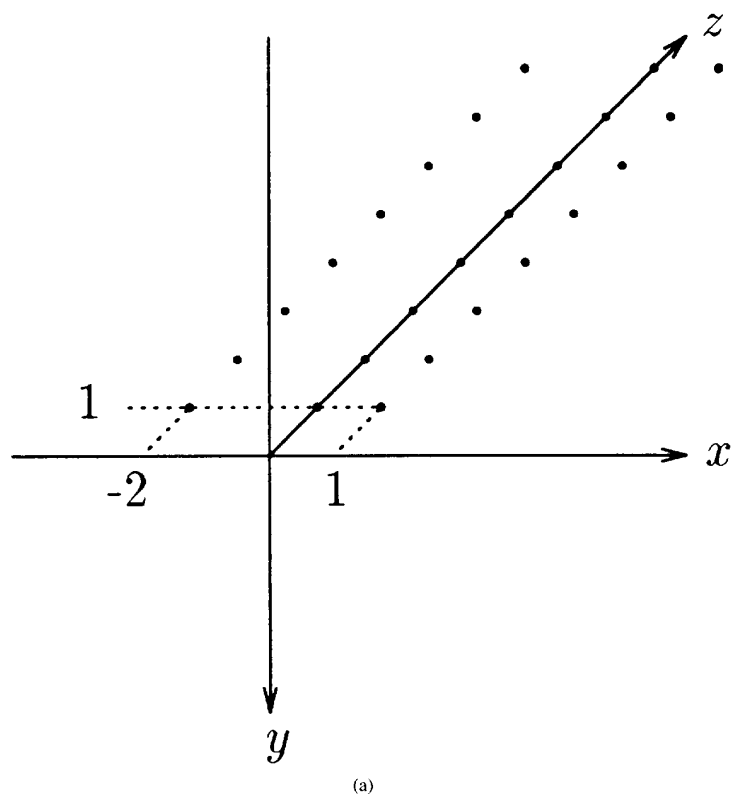
(a)

(b)

Fig. 5.   Reconstruction of a multiple point source. $N = 64, K = 64$. Top: Geometry of source configuration. Lower left: xy-plane at $z = 5$ units. Lower right: zx-plane at $y = 0$.

detector array (10×10 units) assumed. Because of the obvious symmetry in the y-direction, only three zx-planes are shown in Fig. 7.

The computation of the parallel-ray projection by (19) (that is, algorithm 2) has also been implemented numerically and tested. The integral is performed by the midpoint rule with standard Fourier domain techniques used to perform the convolution. Modification of the filter given by (20) is necessary at

high frequencies to obtain reliable reconstruction. The parallel-ray projection as calculated by algorithm 2 is shown in Fig. 8 for a point source located at different distances from the camera and for the three sampling schemes. Generation of the parallel-ray projection for sources near the camera is reliable, but degrades quickly for increasing source distance from the camera. Note too that the projections appear hollow as the source distance increases. This is an artefact due to the missing
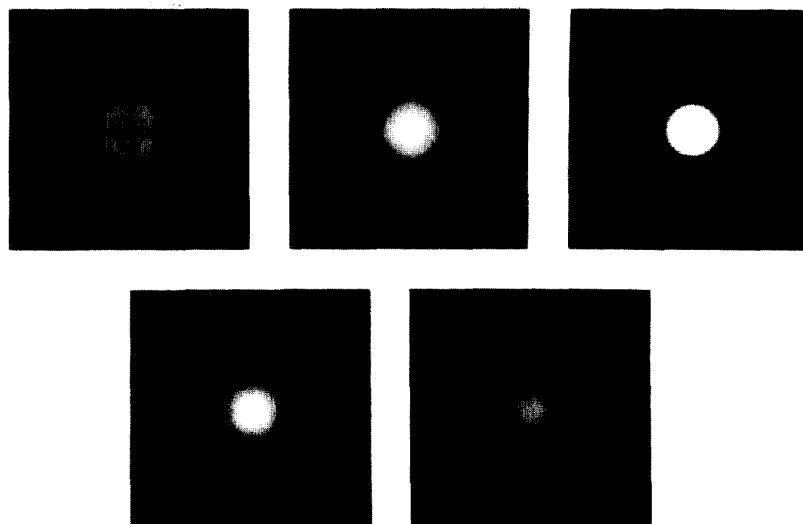
Fig. 6. Reconstruction of a uniform spherical distribution. The sphere has radius $= 1$ unit and is located at $(0.0.5$ units), $N = 64, K = 64$. A variety of xy-planes are shown. In order from top left to bottom right $z = 3.44$, 4.06 (just inside sphere), $5.0.5.94$ (just inside sphere), 6.56 units.
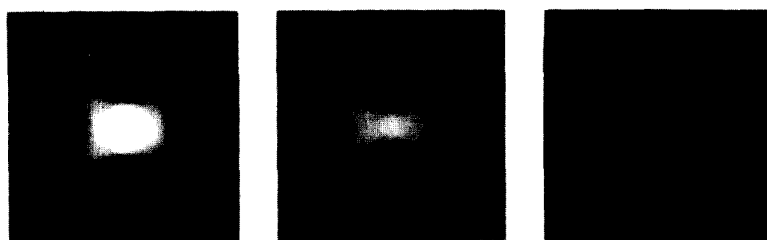

Fig. 7. Reconstruction of a uniform spherical distribution. The sphere has radius $= 1$ unit and is located at $(0.0.5$ units), $N = 64, K = 64$. Several zx-planes are shown. In order from left to right $y = 0.0.0.94$ (just inside sphere), 1.56 units.

data near $t = 0$ (i.e. at very low scattering angles). We are confident that a more realistic treatment for low angles (acknowledging of course that the camera is incapable of measuring data for such angles) can alleviate the artefact in the parallel-ray projections. The circular 'ripples' for the case $N = 64$, $K = 32$ (center row) are an artefact of the discretization model used in the simulation. This is a similar effect to that noticeable in Fig. 4 for the case $N = 64, K = 32$. Unlike the result presented in Fig. 4, introducing blurring to model angular uncertainty does not appear to improve the parallel-ray projection. The process to form the parallel-ray projection may therefore be more susceptible to measurement uncertainties than the complete reconstruction algorithm. We believe a more realistic discretization model may reduce this artefact.

VI. DISCUSSION

The results presented are promising in that they demonstrate that the computer algorithms are capable of providing useful reconstructions for a few simple test sources. To make a comparison with analyses made by other researchers, consider a camera with the same characteristics as that proposed by Singh [4]. Such a camera is a 32×32 element pixellated device with 5×5 mm^2 square pixels giving a total camera area of 16×16 cm^2. To achieve 32 angular samples from $\theta = 0°$ to $\theta = 70°$ would require a detector energy resolution of 300 eV for imaging 140 keV gamma photons. While such an energy resolution is finer than Singh's proposal, it is certainly achievable with current technology. The proposed detector would correspond to the $N = 32$, $K = 32$ simulations reported herein, without photon statistics and measurement uncertainties being considered. The prototype detector, using the first algorithm, would achieve a resolution of 1.6 cm at 5 cm from the detector face and 2.1 cm at 10 cm from the detector face in the xy-plane. In the z-direction the detector would achieve 0.8 cm spatial resolution at 5 cm distance from the first detector face, but at 10 cm distance the spatial resolution has dropped to 2.9 cm. This should be compared to the figure of 1.5 cm (FWHM) predicted spatial resolution [4] and measured 1.5 cm (FWHM) [8] at 10 cm with a prototype device. In making this comparison two things need to be kept
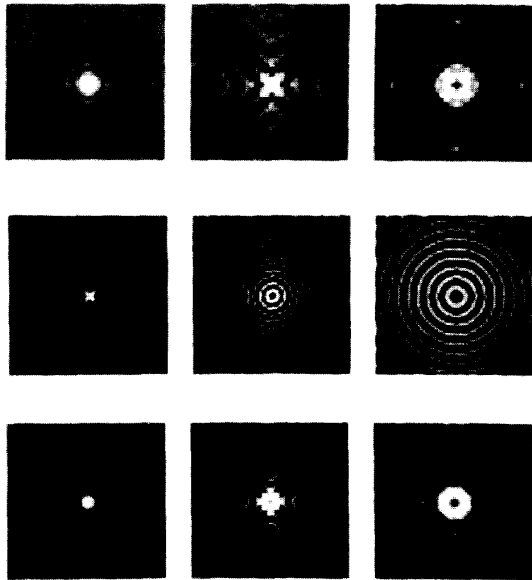
Fig. 8. Calculation of parallel-ray projections from a point source. Top row: $N = 32, K = 32$. Center row: $N = 64, K = 32$. Bottom row: $N = 64, K = 64$. Left column: point source at $(0, 0, 2$ units$)$. Center column: point source at $(0, 0, 4$ units$)$. Right column: point source at $(0, 0, 6$ units$)$.

in mind, namely that Singh & Brechner do consider counting statistics (whereas the simulations presented here do not) and that the algorithm used to generate the results herein is by no means optimal.

It is interesting to note that the Compton scattering camera would seem to offer considerable improvement in performance as the energy of the source is increased. At 500 KeV, for example, the achievable energy resolution corresponds to an angular resolution of the order of 1° (FWHM) at low scattering angles (and less at higher scattering angles), thus the limitations due to limited angular resolution virtually disappear at such higher source energies. The lead collimator of an Anger camera limits the usable energies to those below about 250 KeV [2].

One other feature of the first algorithm is the increasing loss of high frequency Fourier information for increasing z. Some form of compensation is needed so that sources of identical intensity located at various depths can be identified as having identical intensity. For point sources the compensation required can be easily calculated, however compensation for a general source distribution appears more difficult to implement.

The Hankel transform and interpolation stage of the algorithm can be further refined. Obviously, more sophisticated interpolation techniques could be employed but a more interesting alternative would be to modify the Hankel transform algorithm to calculate the transform at arbitrary points rather than on a fixed grid; the need for interpolation can then be avoided at the cost of precluding use of the more computationally efficient FFT-based Hankel transform algorithms.

To achieve an advantage over the Anger camera, it is essential to utilize all available photon detections in the Compton scattering camera. For the first algorithm, this requires ideally that some means of inverting (2) for $\hat{\beta} \neq \hat{z}$ be found. The difficulty seems to be one of incompatible coordinate systems; the integral over the cone surface is essentially based on a cylindrical coordinate system rotated by angle $\hat{\beta}$ with respect to the Cartesian system imposed by the planar detector array. We conjecture that the use of detectors arranged on concentric spherical surfaces may allow an easier treatment to be found. Alternatively there may be some transformation that can be applied to the cone-surface projection data to achieve an invertible version of (2). In lieu of such a rewriting of the problem, there would appear to be opportunities for pragmatic use of approximations. If $\hat{\beta} \cdot \hat{z}$ is small, for example, there is probably no reason why the cone-surface projections should not be treated as though recorded by a detector tilted by the corresponding angle and with slightly modified detector spacing. The set of projections so obtained could be combined to essentially improve the signal-to-noise ratio of the detection process and thus the quality of reconstruction. Note that the approximation is less good for large Compton angle θ so exclusive use of small angle scatter for the off-axis projections is suggested. A similar argument to the above can be invoked to conclude that all detection angles $\hat{\beta} \neq \hat{z}$ are desired to get the best possible image by means of the second algorithm proposed herein. Since the second algorithm computes an alternative projection $p_z(x, y)$ which can be used in reconstruction methods used conventionally (similar to those used in X-ray computed tomography, for example), it is appealing to imagine that it can equally be applied when $\hat{\beta} \neq \hat{z}$. Inspection of (19) however indicates that the convolution necessary to form the parallel-ray projection $p_z(x, y)$ is performed with respect to x and y only. If $\hat{\beta} \neq \hat{z}$, the convolving function must (at least) be modified to take account of the tilted frame of reference; we have not as yet succeeded in establishing how to perform this step.

If attempts discussed above to generalize the algorithms for direct reconstruction fail, there remains the possibility of using the direct reconstruction algorithms to improve iterative schemes. In the schemes of Singh and Doria [6], for example, the set of weights used to relate the sensitivity of a given second plane detector element (with respect to a given detector in the first plane) to a given source point could be altered to reflect the approximate support of the source distribution as derived from the direct method. Many other such schemes to improve iterative reconstruction by means of the direct algorithms seem possible.

It is clear that convincing demonstration of the usefulness of the algorithms presented herein will only come about by their successful use on actual data measured by a Compton scattering camera and/or by the use of simulations which take into account the statistical nature of the photon incidence and detection, the physical properties of the camera components and attenuation within the body under study. We are embarking on the latter course of action with the use of Monte Carlo simulation. We reason that extrapolation beyond present day practical devices is thus possible without huge financial outlay. Ultimately, however, we hope to demonstrate direct reconstruction using actual measured data.

VII. CONCLUSION

The Compton scattering camera, which has found favor in astronomical high energy X-ray imaging, has been proposed for medical imaging by Everett et al. [12] and by Singh [4]. The camera may offer better photon counting statistics than the Anger camera at the cost of more difficult image reconstruction. It is shown herein that from a set of restricted cone-surface projections either the complete source distribution or the equivalent parallel-ray projections can be formed. This suggests two reconstruction paths—either direct reconstruction or reconstruction using cone-beam algorithms. Computer algorithms for the two reconstruction paths have been implemented and tested; for ideal noiseless data the algorithms perform well. The algorithms require modification for practical applications.

ACKNOWLEDGMENT

REFERENCES

[1] H. O. Anger, "Scintillation camera," Rev. Sci. Instr., vol. 29, pp. 27–33, 1958.

[2] S. C. Moore, K. Kouris, and I. Cullum, "Collimator design for single photon emission tomography," Eur. J. Nucl. Med., vol. 19, pp. 138–150, 1992.

[3] J. G. Rogers, D. P. Saylor, R. Harrops, X. G. Yao, C. V. M. Leitao, and B. D. Pate, "Design of an efficient position sensitive gamma ray detector for nuclear medicine," Phys. Med. Biol., vol. 31, pp. 1061–1090, 1986.

[4] M. Singh, "An electronically collimated gamma camera for single photon emission computed tomography. Part I: Theoretical considerations and design criteria," Med. Phys., vol. 10, pp. 421–427, 1983.

[5] R. Diehl, "The COMPTEL experiment on the NASA gamma-ray observatory," Space Sci. Rev., vol. 49, pp. 85–106, 1988.

[6] M. Singh and D. Doria, "An electronically collimated gamma camera for single photon emission computed tomography. Part II: Image reconstruction and preliminary experimental measurements," Med. Phys., vol. 10, pp. 428–435, 1983.

[7] T. Hebert, R. Leahy, and M. Singh, "Three-dimensional maximum-likelihood reconstruction for an electronically collimated single-photon-emission imaging system," J. Opt. Soc. Am. A, vol. 7, pp. 1305–1313, 1990.

[8] M. Singh and R. R. Brechner, "Experimental test-object study of electronically collimated SPECT," J. Nucl. Med., vol. 31, pp. 178–186, 1990.

[9] C. J. Solomon and R. J. Ott, "Gamma ray imaging with silicon detectors—a Compton camera for radionuclide imaging in medicine," Nucl. Inst. and Meth., vol. A273, pp. 787–792, 1988.

[10] H. J. P. Kuykens and S. A. Audet, "A 3×3 silicon drift chamber array for application in an electronic collimator," Nucl. Inst. and Meth., vol. A273, pp. 570–574, 1988.

[11] H. H. Barrett and W. Swindell, Radiological Imaging. The Theory of Image Formation, Detection and Processing. New York: Academic Press, 1981.

[12] D. B. Everett, J. S. Fleming, R. W. Todd, and J. M. Nightingale, "Gamma-radiation imaging system based on the Compton effect," Proc. IEE, vol. 124, pp. 995–1000, 1977.

[13] T. Kamae, N. Hanada, and R. Enomoto, "Prototype design of multiple Compton gamma-ray camera," IEEE Trans. Nucl. Sci., vol. 35, pp. 352–355, 1988.

[14] N. Dogan, D. K. Wehe, and A. Z. Akcasu, "A source reconstruction method for multiple scatter Compton cameras," IEEE Trans. Nucl. Sci., vol. 39, pp. 1427–1430, 1992.

[15] B. D. Smith, "Cone-beam tomography: Recent advances and a tutorial review," Opt. Eng., vol. 29, pp. 524–534, 1990.

[16] G. T. Herman, Image Reconstruction from Projections. The Fundamentals of Computerized Tomography. London, U.K.: Academic Press, 1980.

[17] B. W. Suter, "Foundations of Hankel transform algorithms," Quart. Appl. Math., vol. 49, pp. 267–279, 1991.

[18] M. J. Cree and P. J. Bones, "Algorithms to numerically evaluate the Hankel transform," Comp. Math. Appl., vol. 26, pp. 1–12, 1993.